Article

Scalability and stability in CO_2 reduction via tomography-guided system design

Scalable and durable GDEs

Cu catalyst layer

PTFE-based MPL with porous carbon domain

Colin P. O'Brien, David McLaughlin, Thomas Böhm, ..., Edward H. Sargent, Simon Thiele, David Sinton

si.thiele@fz-juelich.de (S.T.)
dave.sinton@utoronto.ca (D.S.)

Highlights

We develop a gas diffusion electrode resistant to flooding and stable for >400 h

We create a digital model of the electrode to determine transport properties

We scale this approach in an 800 cm^2 cell and an 8,000 cm^2 stack

We show the largest CO_2 electrolysis demonstration reported to date (>10^6 C)

There have been significant advances in CO_2 electrolyzers; however, achieving stability remains a challenge. Here, we develop a stable and scalable electrode substrate that is resistant to flooding and operates for more than 400 h without loss of performance. Using transport modeling from tomographic reconstruction, we develop large-scale electrodes that operate with stable performance in an 8,000 cm^2 stack.

Joule

Article

Scalability and stability in CO_2 reduction via tomography-guided system design

Colin P. O'Brien,[1,5] David McLaughlin,[2,3,5] Thomas Böhm,[2] Yurou Celine Xiao,[1] Jonathan P. Edwards,[1] Christine M. Gabardo,[1] Markus Bierling,[2,3] Joshua Wicks,[4] Armin Sedighian Rasouli,[4] Jehad Abed,[4] Daniel Young,[1] Cao-Thang Dinh,[4] Edward H. Sargent,[4] Simon Thiele,[2,3,*] and David Sinton[1,6,*]

SUMMARY

Electrocatalytic CO_2 reduction offers a means to produce value-added multi-carbon products and mitigate CO_2 emissions. However, the stability of CO_2 electrolyzers for C_{2+} products has not exceeded 200 h—well below that of CO- and H_2-producing electrolyzers—and the most stable systems employ low-conductivity substrates incompatible with scale. Current gas diffusion electrodes (GDEs) become filled with salt precipitate and electrolyte, which limits CO_2 availability at the catalyst beyond 30 h. We develop a GDE architecture that is resistant to flooding and maintains stable performance for >400 h. Using a combination of focused ion beam scanning electron microscopy, micro-computed tomography, and a purpose-built array tomography technique, we determine that the enhanced stability is due to a percolating network of polytetrafluoroethylene in the microporous layer that retains hydrophobicity. We scale this approach in an 800 cm^2 cell and an 8,000 cm^2 stack and transfer >10^8 C, the largest reported CO_2 electrolysis demonstration.

INTRODUCTION

The CO_2 reduction reaction (CO_2RR) is a promising route to produce value-added chemicals from CO_2 and renewable electricity.[1] Of the many possible CO_2RR products, multi-carbon (C_{2+}) products such as ethylene (C_2H_4) and ethanol (C_2H_5OH) are particularly attractive in view of their high value and large market size.

Gas diffusion electrodes (GDEs) can be integrated into CO_2 electrolyzers to decrease CO_2 diffusion barriers and increase reaction rates to industrially relevant current densities—those greater than 100 mA/cm². These high reaction rates are required to reduce electrolyzer capital costs.[2–4] GDEs are generally comprised of a gas diffusion layer (GDL) and the catalyst layer (CL). The GDL provides a gas-permeable substrate to support the CL, such as carbon paper, carbon cloth, or expanded polytetrafluoroethylene (PTFE) membrane.[5] Carbon-based GDLs typically include a microporous layer (MPL)—the MPL is a porous electrically conductive hydrophobic layer that controls the gas-liquid boundary. The porosity of the MPL allows gas to diffuse rapidly from the GDL to the CL, while the hydrophobicity and small pore size of the MPL prevent electrolyte flooding.

GDEs for CO_2RR, along with all cell components, must be able to demonstrate stable performance for at least 10,000 h in order to make material and replacement costs acceptably low for commercial implementation.[2,4,6] There are several stable demonstrations of CO_2RR to carbon monoxide (CO) reported for durations longer

CONTEXT & SCALE

The rising atmospheric CO_2 concentration has motivated research into alternative methods to supply the world's most important chemicals and fuels. The electrochemical CO_2 reduction reaction is a promising route to utilize increasingly abundant renewable electricity to produce low-carbon-intensity fuels and chemicals.

There have been significant advances in CO_2 electrolyzers; however, achieving operational stability sufficient for industrial applications remains a challenge. Currently, there have been no demonstrations of stable production of C_2 products for >200 h, and the most stable systems employ low-conductivity substrates incompatible with scale. Here, we develop a stable and scalable electrode substrate that is resistant to flooding and operates for more than 400 h without loss of performance. Using transport modeling from tomographic reconstruction, we develop large-scale electrodes that operate with stable performance in an 8,000 cm^2 stack.

than 1,000 h.[7–11] However, to date, there have been no demonstrations of stable performance (with a current density >100 mA/cm^2) for the CO_2RR to C_{2+} products for more than 200 h.[12–14] The conversion of CO_2 to C_{2+} products poses additional stability challenges due to the instability of copper-based catalysts[15] and the interaction of liquid CO_2RR products with cell components.[16] So far, GDEs fabricated on PTFE-based GDLs have shown the best stability for CO_2RR to C_{2+} products.[14,17,18] However, these GDLs are restricted to small reaction areas because they are only electrically conductive within the thin plane of the CL. The large currents required in large cells—greater than 100 A for an 800 cm^2 cell—require GDLs that are conductive in the through-plane direction to minimize the electrode's ohmic resistance.

The conductive commercial carbon-based GDLs designed for fuel cell applications provide sufficient electrical conductivity but suffer from poor long-term stability when used for CO_2RR to C_{2+} products. Fuel cell electrodes are designed to be hydrophobic to prevent flooding with liquid water, but the high electrolyte concentrations[19–21] and low surface tension liquid products[22] present in CO_2RR systems result in liquid penetration and salt precipitation. Once the electrode is flooded, the CO_2 diffusion pathways to the catalyst are blocked, and the hydrogen evolution reaction (HER) occurs on the carbon-based GDL.[23] New GDEs that can simultaneously support large currents and resist flooding are essential for the scale-up of CO_2RR to C_{2+} technology and the maturation of this field.

To understand the performance and failure modes of the GDE, it is necessary to first analyze their physical structure. This structural characterization can be accomplished through the tomography of the electrode. A unique challenge arising in the tomography of GDEs is their multiscale nature, with key features spanning the nano- and micro-scale domains. The standard method to analyze porous structures, such as catalyst and MPLs, is focused ion beam scanning electron microscopy (FIB/SEM).[24–26] However, FIB/SEM cannot cover all relevant length scales in a GDE—for instance, the fibers of the GDL at the micrometer scale are too large to be imaged with this technique. The larger field of view offered by micro-computed tomography (microCT) of GDEs cannot resolve the nanoporous domains.[27] Therefore, multi-modal tomography is required to obtain a full digital model of a GDE, a representative 3D reconstruction of the GDE encompassing all relevant length scales. In earlier works, we showed that the combination of FIB/SEM and microCT can be used to create a digital model of a CO_2 electrolysis GDE.[28] Similarly, fuel cells[29,30] and batteries[31] have been studied by means of multiscale tomographic analysis.

Here, we begin from a membrane electrode assembly (MEA) cell with commercial carbon-based GDLs and a Cu nanoparticle CL. We demonstrate that the commercial carbon-based GDLs are not stable over an initial 30 h experiment as the faradaic efficiency (FE) toward the HER increases at the expense of CO_2R. Cross-sectional energy-dispersive X-ray (EDX) mapping confirms that the poor stability is due to salt crystallization and flooding in the MPL—both of which hinder CO_2 diffusion to the catalyst. To improve the stability, we develop a scalable segregated GDL with enhanced hydrophobicity that reduces electrolyte penetration and is stable for 400 h—the longest demonstration of CO_2R to C_{2+} products to date. To demonstrate enhanced PTFE-carbon domain separation within the MPL, we develop a new array tomography approach that resolves the percolating network of PTFE and the nanoporous carbon domains. A digital model built from the imaging data is used to calculate its transport properties, confirm the rational design, and elucidate the observed stability in cell testing. Applying this approach, we scale the GDE to an 800 cm^2 cell

[1]Department of Mechanical and Industrial Engineering, University of Toronto, Toronto, ON M5S 3G8, Canada

[2]Forschungszentrum Jülich GmbH, Helmholtz Institute Erlangen-Nürnberg for Renewable Energy (IEK-11), 91058 Erlangen, Germany

[3]Department of Chemical and Biological Engineering, Friedrich-Alexander-Universität Erlangen-Nürnberg, 91058 Erlangen, Germany
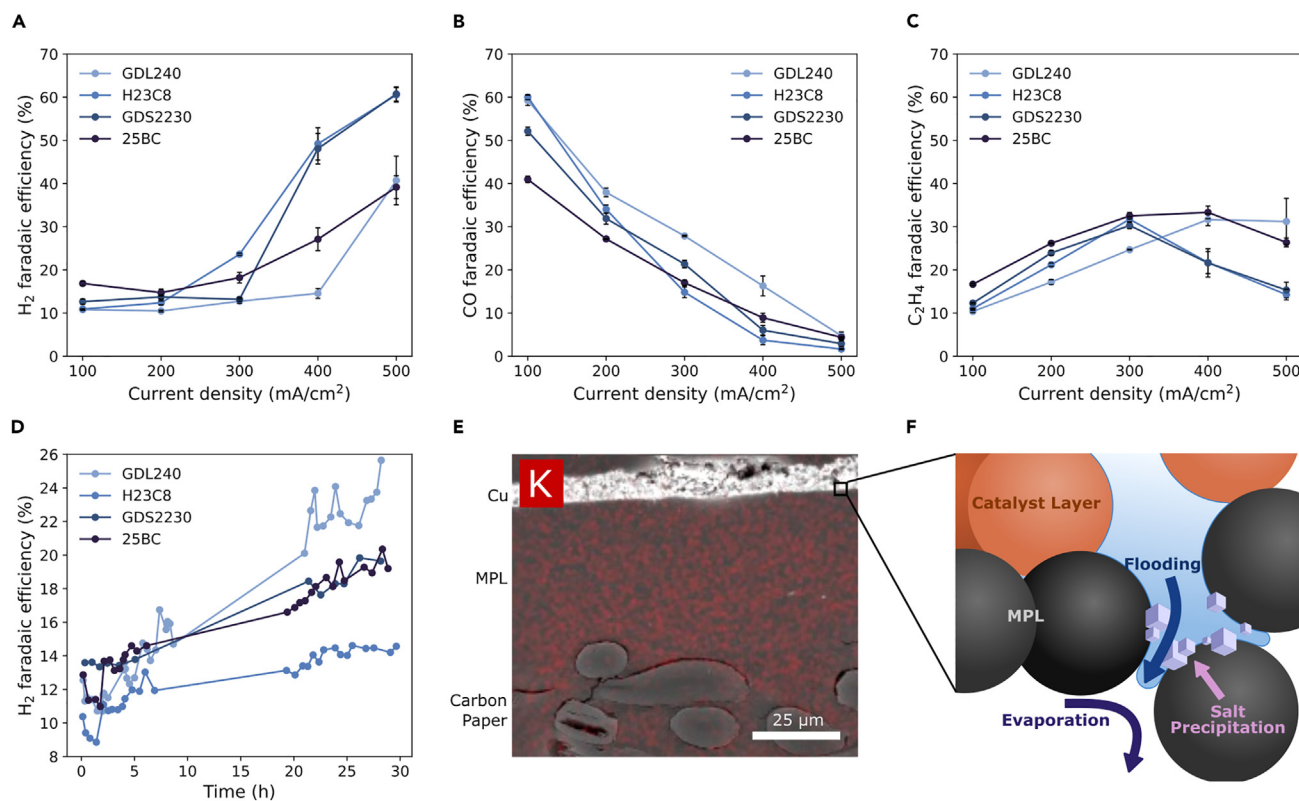
[4]Department of Electrical and Computer Engineering, University of Toronto, Toronto, ON M5S 1A4, Canada

[5]These authors contributed equally

[6]Lead contact

*Correspondence: si.thiele@fz-juelich.de (S.T.), dave.sinton@utoronto.ca (D.S.)

https://doi.org/10.1016/j.joule.2024.07.004

Figure 1. Electrochemical performance of GDEs based on commercial GDLs

(A–C) Faradaic efficiency as a function of current density for commercial carbon-based GDLs for (A) H_2, (B) CO, and (C) C_2H_4. Error bars represent the standard deviation of at least 3 independent measurements.

(D) Stability of H_2 faradaic efficiency at 200 mA/cm^2 for commercial carbon-based GDLs with automatic DI water rinsing every 2 h (gas product distribution in Figure S2).

(E) Cross-section SEM-EDX micrograph of the H23C8-based GDE after continuous operation for 30 h at 200 mA/cm^2 with the K signal overlayed in red.

(F) Schematic demonstrating the flooding mechanism in commercial carbon-based GDLs.

and a 10-cell 8,000 cm^2 stack and operate each for 240 h—the largest demonstration of CO_2RR to C_{2+} products reported to date.

RESULTS AND DISCUSSION

Commercial carbon paper-based GDEs

We assembled an MEA cell with commercial carbon-based GDLs (details in Table S1), sprayed with a Cu nanoparticle CL with a carbon black catalyst support, an anion-exchange membrane (Sustainion X37–50), and an IrOx on titanium felt anode. The Cu CL is bound with a Nafion perfluorosulfonic acid (PFSA) ionomer that increases the CO_2 transport in the CL.[32] The carbon black catalyst support is bound with an anion-exchange ionomer (Sustainion XA-9) to increase the anion conductivity and transport through this catalyst overlayer.[7] We evaluated the gas product selectivity and the voltage response of each commercial carbon-based GDL at current densities between 100 and 500 mA/cm^2. At 100 and 200 mA/cm^2, the H_2 FE was low, less than 17%, for all GDLs (Figure 1A). As the current density was increased to 300, 400, and 500 mA/cm^2, the H_2 FE increased to greater than 30%, presumably because CO_2 mass transport limits were reached. The commercial GDLs reached these limitations at different current densities due to their differences in gas permeability and hydrophobicity. Each GDL showed CO FE decreasing with

current density—an effect we attribute to an increase in local pH at the catalyst.[17,33,34] The increased local pH is both due to the increased production of OH^- at higher current densities and the decreased local CO_2 concentration, which decreases the rate of reaction of CO_2 with OH^-.[35,36] At higher current densities, C_2H_4 production was favored over CO production (Figure 1C); however, the selectivity for C_2H_4 decreased as CO_2 mass transport limits were reached in each case.

The predominant drawback of the commercial carbon-based GDLs is their lack of stability during CO_2RR due to electrode flooding and the accumulation of salt. We evaluated stability while periodically rinsing the back of the GDE with deionized (DI) water to mitigate salt precipitation. The rinsing was performed with a peristaltic pump controlled by an automatic timer that fed the water into the CO_2 inlet for 1 min every 2 h, while the cell was running (stability without rinsing is shown in Figure S1). In stability experiments at 200 mA/cm², each GDL experienced an increase in H_2 FE over 30 h. The most stable GDL, Freudenberg H23C8, experienced an increase in H_2 FE from 9% to 14% over the 30 h experiment (Figure 1D). This increase in H_2 FE over the first 30 h—even with periodic rinsing—highlights the gap between current performance levels and commercial viability; 10,000 h of stable operation with less than 10% of performance degradation.[12]

Using cross-sectional SEM and EDX, we identified the precipitation and dense accumulation of potassium-based salts (Figure 1E) as a primary source of instability. During operation, it is expected that the hydrophilic CL is hydrated due to the humidification of the CO_2 gas feed and the diffusion of water through the high water uptake anion-exchange membrane.[37–39] This liquid layer contains K^+ cations that diffuse from the anolyte and OH^-, CO_3^{2-}, and HCO_3^- from CO_2RR and the reaction of CO_2 with OH^-. The liquid products of CO_2R can reduce the contact angle of the liquid electrolyte in the CL[40] and lead to electrolyte penetration into the GDL (Figure 1F). Water is also consumed in the CO_2RR and lost through evaporation into the gas stream. As a result, the concentration of ions increases, and $KHCO_3$ and $K_4H_2(CO_3)_3 \cdot 1.5\,H_2O$ salts[20,21] precipitate when the solubility limit is reached. The hydrophilic salts precipitate along the pore walls of the MPL, which reduces its hydrophobicity, inducing further flooding.[20,21] The periodic rinsing reduces the rate of salt accumulation but does not eliminate it. Throughout the 30-h experiment, the concentration of CO_2 available at the catalyst was steadily reduced, which resulted in an increase of the HER.

A segregated GDL for stable CO_2 reduction

We sought a new GDL architecture that would be resistant to salt precipitation while retaining electrical conductivity in the through-plane direction. We engineered a custom, segregated domain MPL design that contains flooding-resistant and salt precipitation-resistant hydrophobic PTFE domains. In this MPL, the PTFE domains are intended to maintain hydrophobicity, while the carbon domains ensure electrical conductivity and gas transport.

We replaced the commercial GDL in the cell with the segregated GDL with a high PTFE content MPL and measured the electrochemical performance. At 100 mA/cm², the segregated GDL had a 50 mV voltage penalty compared with the best commercial GDL (Figure 2A). The voltage penalty was likely caused by a decreased electrical conductivity owing to the high PTFE content of this GDL: the segregated PTFE and carbon domains of the MPL result in fewer conduction pathways compared with the commercial GDL. As the current density was increased to 300, 400, and 500 mA/cm², the cell voltage of the segregated GDL was less than the cell voltage of the
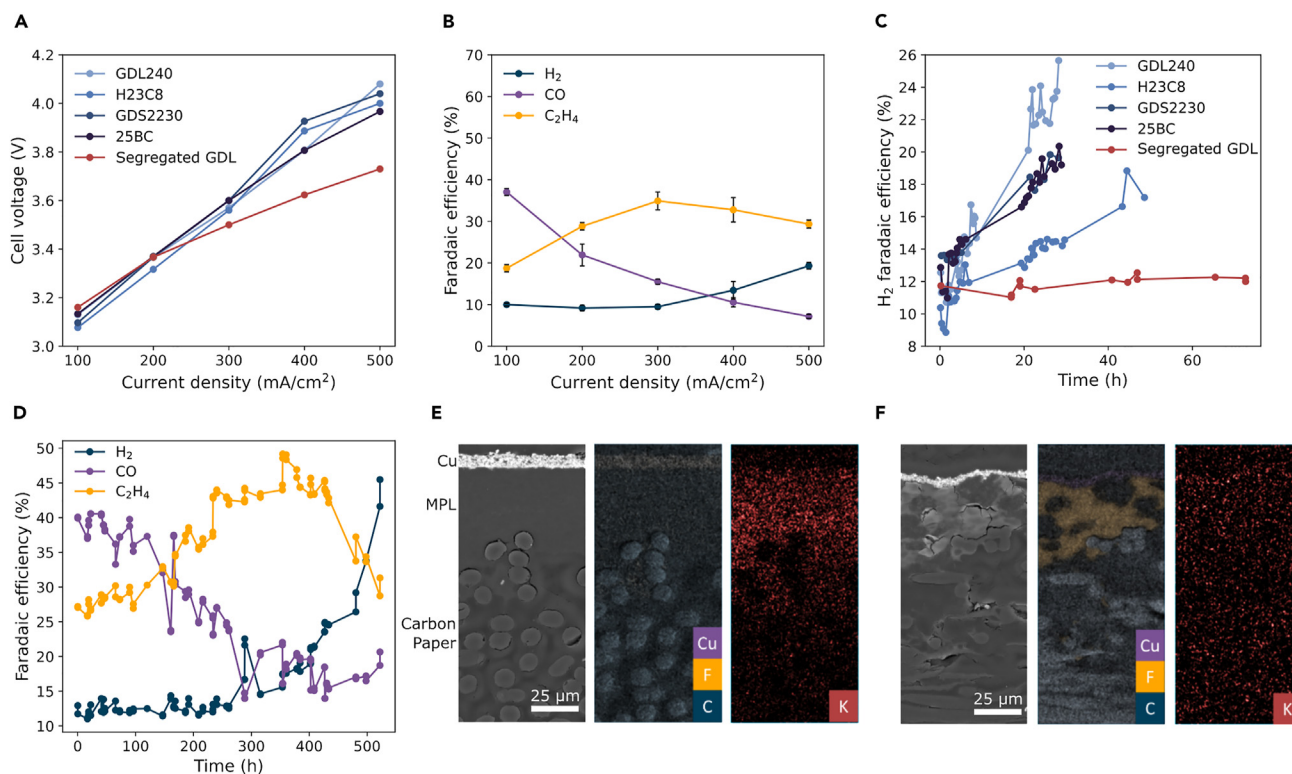
Figure 2. Electrochemical performance of the segregated GDL

(A) Cell voltage as a function of the applied current density for the commercial and the segregated GDLs.

(B) Gas product faradaic efficiency (FE) as a function of current density for the segregated GDL (liquid product FEs are available in Figure S5). Error bars represent the standard deviation of at least 3 independent measurements.

(C) Stability comparison of the H_2 FE at 200 mA/cm^2 for the commercial and the segregated GDLs.

(D) Stability of gas product FE at 200 mA/cm^2 for the segregated GDL.

(E and F) Cross-section SEM-EDX of the (E) H23C8 GDE and the (F) segregated GDL after continuous operation for 30 h at 200 mA/cm^2 with the SEM micrograph displayed on the left panel, the C, F, and Cu signals displayed on the center panel, and the K signal displayed on the right panel.

commercial GDLs. The decreased voltage at higher current densities is attributed to improved CO_2 mass transport and reduced GDL flooding, which was supported by the decreased H_2 FE compared with the commercial GDLs (Figures 2B and 1A). At 500 mA/cm^2, the cell voltage and H_2 FE of the segregated GDL were 270 mV and 20% lower than the best performing commercial GDL. Using electrochemical impedance spectroscopy (EIS), the enhanced CO_2 mass transport of the segregated GDL was further confirmed by the decreased mass and charge transfer resistance at 400 and 500 mA/cm^2 compared with the H23C8 GDL (Figure S3). The enhanced mass transport of the segregated GDL also allows it to perform the CO reduction reaction (CORR) at similar reaction rates (Figure S4), despite the low solubility of CO in aqueous solutions.

To evaluate the durability, we measured the H_2 FE of the segregated GDL over time and compared it to the same measurement of the commercial GDLs (Figure 2C). The segregated GDL showed the lowest increase in H_2 FE, only 1% over 72 h. We then measured the performance of the cell at 200 mA/cm^2 over 500 h (Figure 2D). The H_2 FE remained below 15% for more than 280 h of operation. This improvement corresponds to an order of magnitude increase in stability compared with the best commercial GDL. During the experiment, the C_2H_4 FE increased until 360 h, while the CO FE decreased accordingly. We hypothesized that small amounts of salt deposited in

CellPress
OPEN ACCESS

Joule
Article

the CL and the MPL over time, decreasing CO$_2$ availability at the catalyst, and resulting in a higher local pH that is favorable for C–C coupling. We confirmed that the enhanced stability of the segregated GDL is due to better resistance to flooding and less accumulation of salt, which was shown by the low K EDX signal after 30 h of operation (Figures 2E and 2F). The increased PTFE content in the segregated MPL is also evident from the intensity of the F signal in a cross-sectional EDX scan when compared with a commercial GDL. After the peak ethylene FE of 49% was reached at the 360 h mark, continued salt accumulation may have resulted in increased flooding of the GDL with electrolyte, which then substantially hindered CO$_2$ transport to the CL and led to a decrease in ethylene FE and an increase in H$_2$ FE. Although the segregated GDL mitigates salt precipitation within the MPL and carbon paper substrate, the structural properties that bring this about cannot be resolved with conventional 2-dimensional techniques.

Tomographic analysis

The long-term stability of the segregated GDL suggests a fundamental difference in structure compared with commercial GDLs, which we probed via tomography. A three-pronged approach was taken to address the issue of the different length scales within this type of sample: the pores in the CL are on the nanometer scale, while the fibers of the carbon paper GDL are on the micrometer scale. FIB/SEM tomography was used to reconstruct the nanoporous carbon and copper domains. A new EDX-array tomography approach was developed in this work to analyze the PTFE matrix of the MPL. This method was necessary to achieve high contrast between carbon and PTFE in the presence of copper at all relevant scales. X-ray-based techniques cannot resolve the large differences in specific absorption between copper, PTFE, and carbon. The array tomography approach offers chemical sensitivity through the EDX mapping of serial sections of the sample, which can be used to create a 3D model. Finally, the structure of the carbon paper GDL was resolved using microCT. The combined process is illustrated in Figure 3. The 3D reconstruction produced a multiscale model of all key regions of the GDE, which was used to differentiate the GDE's structural properties. This digital model of the electrode replicates the GDE structure closely and offers the flexibility of digital analysis, simulation, and modification.

The structure resolution capabilities of the multiscale tomography are demonstrated in Figure 4. The carbon paper substrate is composed of fibers and a hydrophobic binder (Figure 4E), and the new MPL is sandwiched between the carbon paper substrate and CL. This MPL consists of carbon domains (approximately two-thirds of the volume) with interpenetrating PTFE (Figure 4B) (approximately one-third). Due to the fabrication technique, this type of MPL differs fundamentally from those found in commercial carbon papers. MPLs typically used for CO$_2$RR feature a hydrophobicity enhancing treatment, for instance, by the addition of PTFE (see fluorine signal in Figure 1E). However, in the segregated MPL, the additional hydrophobicity is provided by a percolating network of PTFE, which prevents flooding and salt precipitation. The success of the design is thus not only due to the high PTFE content but also to the two-domain distribution. A well-dispersed single-domain MPL with high PTFE content would be less electrically conductive. The mean diameter of the PTFE network's grains is 4 μm, whereas the porous carbon superstructure averages 7 μm. The carbon domain in the MPL provides access to reactants through its high porosity (almost 80%). The mode of the pore-size distribution (Figure 4F) falls at 130 nm, matching that of the catalyst (Figure 4A), indicating that the transport of reactants and products is similar in the MPL and the CL. The CL porosity is likely to be overestimated, as we could not detect the Nafion binder in the CL. We have investigated

Joule
Article

CellPress
OPEN ACCESS
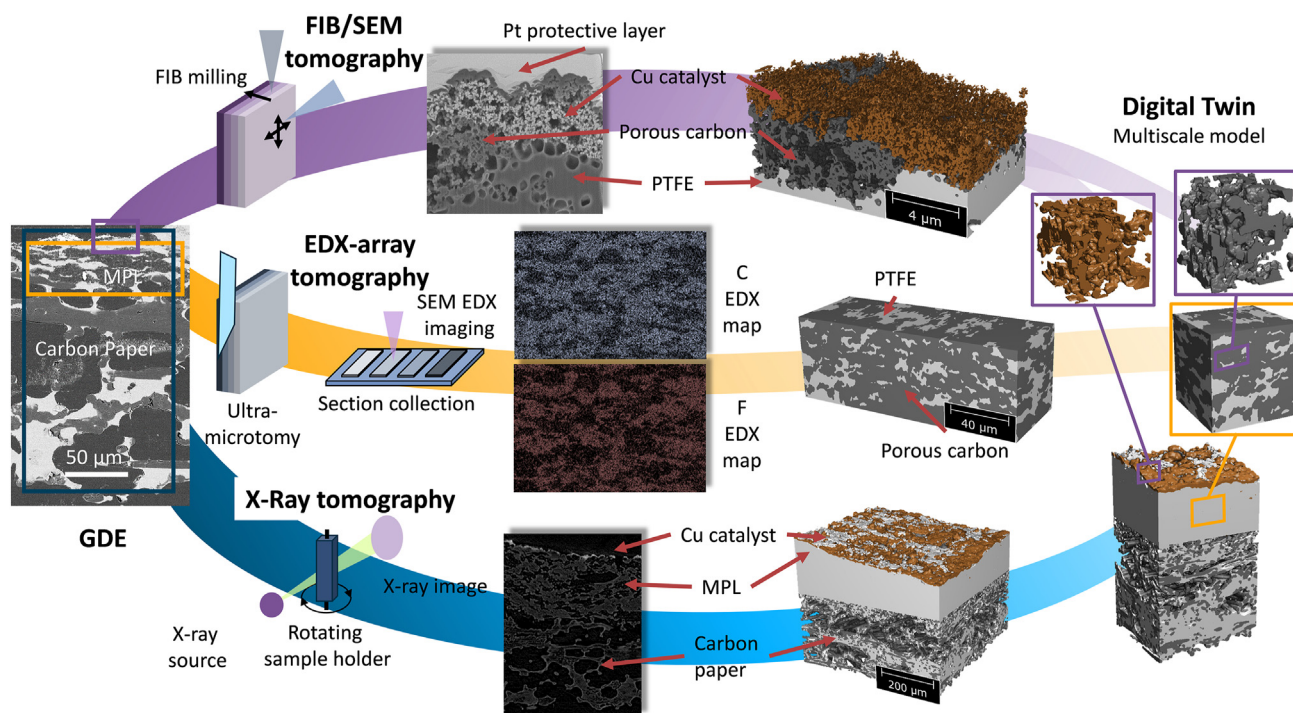
Figure 3. Multi-modal tomographic approach featuring a combination of FIB/SEM tomography, EDX-array tomography, and X-ray tomography

This combination of tomographic techniques allows for the complete resolution of the GDE. Excerpts of the reconstructions are shown in Figures 3, 4, and 5. Visualizations can also be found in the supplemental information in Figures S6–S8 and S10–S13. The size of the full reconstructions is documented in Table S5.

the effect of Nafion on the pore space and the resulting changes to the pore-size distribution in a modeling study (more details in Figures S15 and S18).

The multiscale nature of our reconstruction enables the study of the porosity across divergent scales. Figure 4D shows that the GDE exhibits a strongly bimodal pore-size distribution. The micropores of the GDL form one peak with the largest volume fraction attributed to pores on the 20–30 μm scale. The MPL and, to a lesser degree, the CL contribute a large volume of sub-micron pores. The structure of the digital model of our GDE suggests a transport path through the nanoporous carbon domain of the MPL.

We investigated various transport processes (diffusion, electronic conduction, and fluid flow) in the reconstructed volumes of the electrode and compared them to the results of a conventional GDE via its digital model (Figure 5). The two-domain nature of the segregated MPL is compared with a commercial GDE with a single-domain MPL.[28] The commercial GDE is based on a Freudenberg H23C2 from a previous work[28] and closely matches the H23C8-based GDE shown above. The differences in structure between C2 and C8 seem to be minor (see Figure S9). Visualizations for the results of the simulated transport processes are shown in Figures S10–S13. We expect structural differences between the structures of a GDE measured *ex situ* compared with the GDE in a compressed state. However, the GDE samples in the post mortem analysis (Figures 2E and 2F) appear to be similar to the samples before reaction, which indicates that the structures are mostly intact during operation. The transport parameters in Figure 5 are given for the through-plane direction as material- and species-independent relative conductivities and
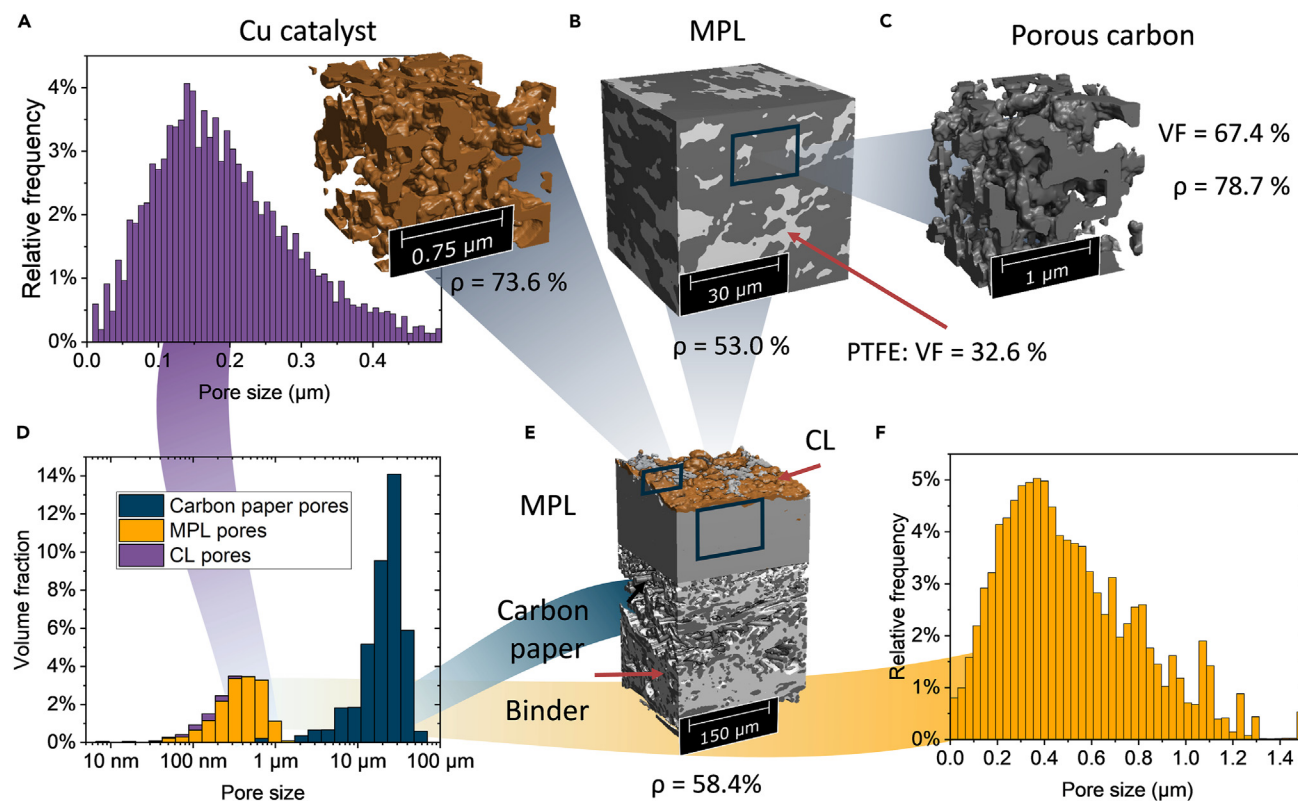
Figure 4. Visualization of the GDE based on excerpts of the multiscale tomography

(A) The pore-size distribution, along with a visualization of the copper CL.

(B) Reconstruction of the MPL structure showing the distribution of PTFE and porous carbon.

(C) Reconstruction of the porous carbon domain.

(D) Overall pore-size distribution of the GDE.

(E) Reconstruction of the GDE by microCT with indicated locations of the main components.

(F) Pore-size distribution of the porous carbon domain of the MPL. VF, volume fraction; ρ, porosity.

diffusivities (the transport parameters in the other directions, the estimated errors, and the computed effective parameters can be found in the supplemental information (Tables S3 and S4). The CL transport parameters likely overestimate the available pore space. More details are available in Figures S15–S17.

Compared with a commercial carbon paper GDE, the two-domain MPL and the interpenetrating network of PTFE in the segregated GDE result in decreased Laplace and Knudsen diffusivities (Figure 5). While the porous carbon domain of the MPL features higher diffusivities than commercial porous carbon, the diffusion and conduction pathways are longer due to the interpenetrating domains. The diffusion pathways are likely well protected from flooding by the hydrophobicity of the surrounding PTFE matrix, which matches the improved long-term stability and reduced mass transport losses at high current densities of the custom GDE. The permeabilities are slightly higher for the segregated MPL and lower for the carbon paper with respect to the conventional system. The drop in permeability can be attributed to the hydrophobic treatment of the carbon paper. However, the models indicate a difference in the conductivity, 10.7% versus 1.8%, and this could account for the voltage penalty of the custom GDE compared with the commercial GDLs at 100 and 200 mA/cm^2 in Figure 1A. It should be noted that these transport coefficients may improve the accuracy of electrochemical continuum models of electrodes

Joule
Article

CellPress
OPEN ACCESS
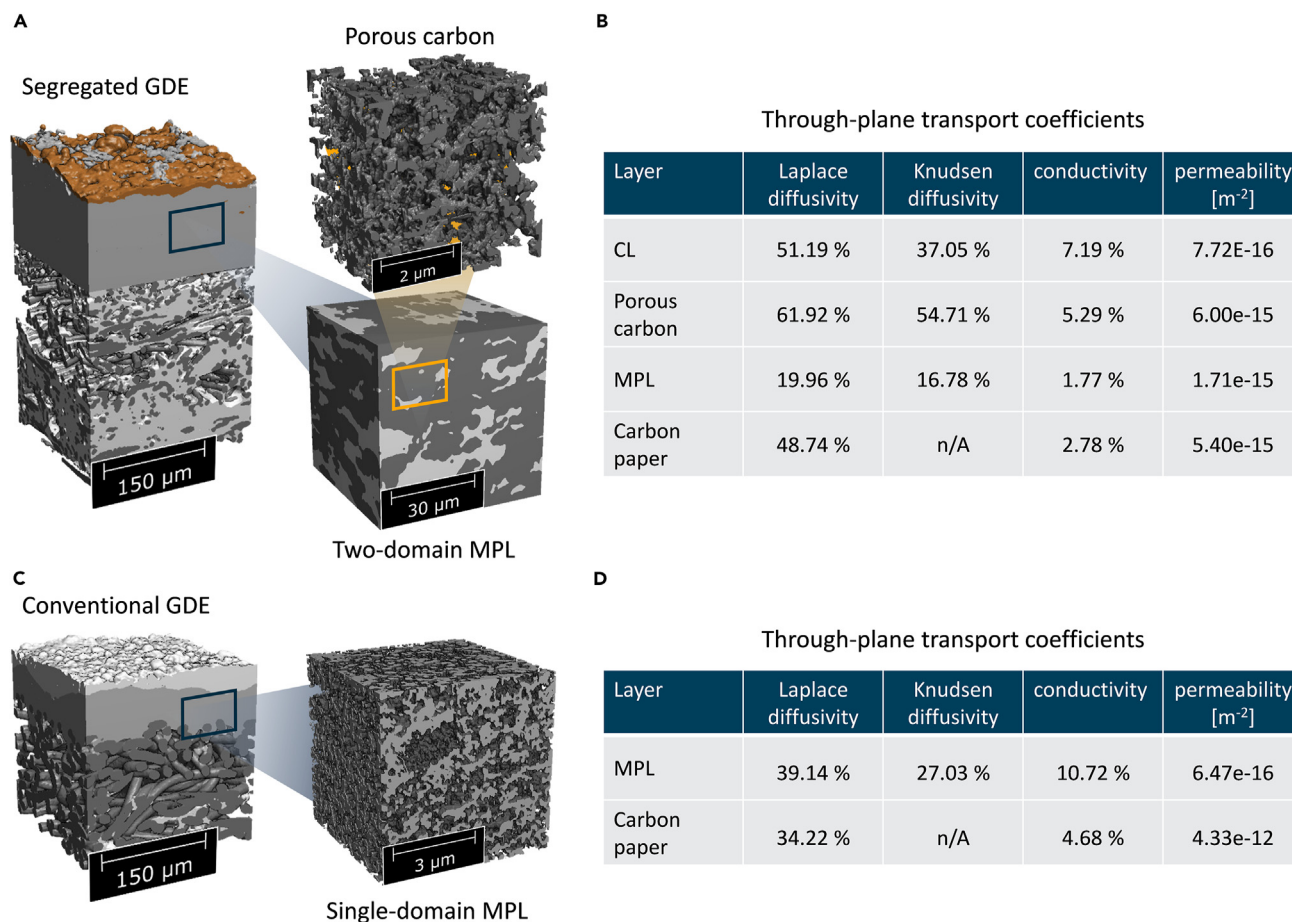
Figure 5. Side-by-side comparison of the structure and transport parameters of the segregated GDE and a conventional GDE
(A) Visualization of the segregated GDE showing the structure of the MPL.
(B) Transport coefficients for the segregated GDE (the direction of computation is the through-plane direction in all cases).
(C) Comparison to a conventional GDE (based on Freudenberg H23C2).
(D) Reference transport parameters for the commercial GDE. We have omitted the values for the CL, as it differs in manufacturing process and material. The conductivity measures the relative conductivity of each layer compared with non-porous carbon and copper. The diffusivities measure the diffusivity compared with an empty volume. Effective diffusivities and conductivities can be found in Table S4. Data of (C) and (D) from McLaughlin et al.[28]

and cells, as these models use approximations for the transport coefficients.[36,41–43] The tomographic findings suggest that during scale-up the thickness of the MPL could be decreased compared with a conventional MPL. Thus, the lower diffusivity could be compensated by overall shorter diffusion pathways.

Scaling

Applying these insights, a 25% thinner MPL was deposited onto the carbon paper substrate to improve gas transport and conduction. This GDL architecture was then scaled to an 800 cm^2 cell (Figure 6A). The single cell was stable for 10 days, 240 h of stable operation at 100 A (125 mA/cm^2) (Figure 6B). We then applied this approach in an 8,000 cm^2 10-cell stack and achieved 240 h stability at 800 A (100 mA/cm^2) (Figure 6C). With a total charge transfer of 6.9 × 10^8 C, this is the largest CO_2 electrolysis demonstration reported in the literature to date, exceeding by 5-fold the previous value of 1.4 × 10^8 C (300 cm^2 at 200 mA/cm^2 for 650 h).[10] The H$_2$ FE remained constant at 50% to 60% throughout the full operation time of the systems. The differences in selectivity between the 5 cm^2 and the 800 cm^2 cells
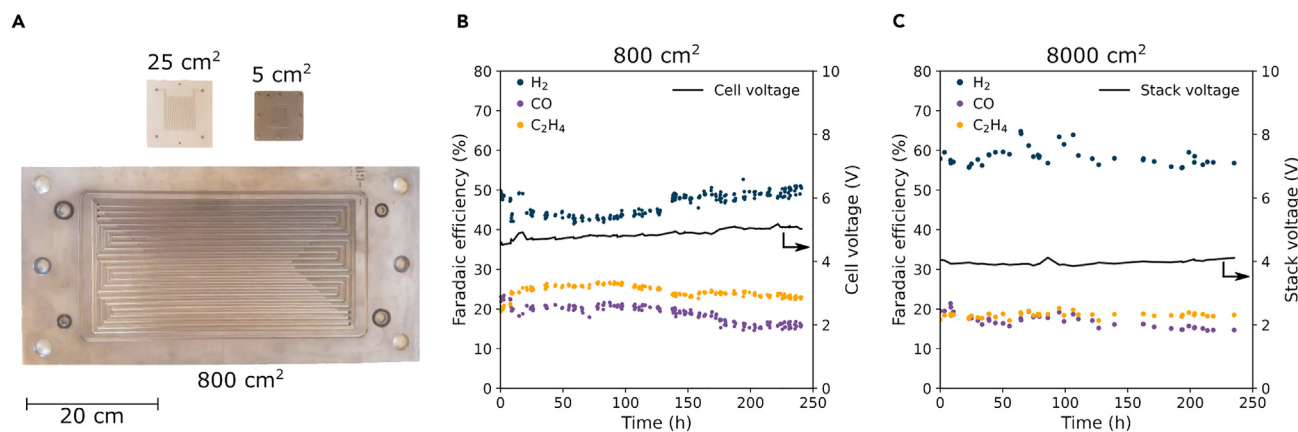
Figure 6. Pilot-scale operation of the segregated GDL
(A) Size comparison of 5, 25, and 800 cm^2 cells.
(B) Stability of an 800 cm^2 cell with the segregated GDL at 100 A (125 mA/cm^2).
(C) Stability of a 10-cell stack of 800 cm^2 cells (8,000 cm^2 total active area) with the segregated GDL at 800 A (100 mA/cm^2).

can be explained by the poor CO$_2$ distribution and mass transport throughout these initial large cell and stack designs (stability of the H23C8 cathode in the 800 cm^2 cell is shown in Figure S19, and the selectivity of the segregated GDL in the 25 cm^2 cell is shown in Figure S20). To reduce HER in the 800 cm^2 cells, the flow field design for gas supply and product removal requires further optimization. However, the consistent selectivity and cell voltage of both scaled experiments confirm the stability and scalability possible in CO$_2$ reduction.

Conclusions

We developed a segregated GDE for CO$_2$ reduction that demonstrates stable performance over several hundred hours of operation and is scalable for usage in cells and stacks with pilot-scale dimensions. The approach of implementing a percolating PTFE network within the MPL of a GDE prevented flooding and increased the CO$_2$RR FE at high current densities. This segregated GDE showed less than 1% increase in FE toward H$_2$ over an initial 72 h test and did not show any signs of degradation until 280 h of operation—a 10× improvement compared with commercial GDLs. Using a three-pronged approach of FIB/SEM, microCT, and a newly developed array tomography technique, we performed a multiscale tomography of the segregated GDE. We developed a digital model of the GDE to model the structural properties and extracted the diffusion, conductivity, and permeability coefficients. The tomogram verified the percolating PTFE network within the MPL of the GDL, and the calculated parameters confirmed that the new GDL layout does not significantly suffer from losses of diffusivity or permeability compared with a commercial GDL. The scalability of the segregated GDL approach is demonstrated through 240 h of stable operation in an 800 cm^2 cell and an 8,000 cm^2 10-cell stack. The 6.9 × 10^8 C of charge transferred during the experiment is the largest CO$_2$R demonstration reported to date. This GDL architecture addresses the coupled challenges of stability and scaling that had limited the field of electrochemical CO$_2$ conversion into multi-carbon products.

EXPERIMENTAL PROCEDURES

Resource availability

Lead contact

Further information and requests for resources should be directed to and will be fulfilled by the lead contact, David Sinton (dave.sinton@utoronto.ca).

Joule
Article

Materials availability

All unique materials generated in this study are available from the lead contact on reasonable request.

Data and code availability

The data supporting the findings of this study are available within the article and its supplemental information. Additional data are available from the corresponding authors on reasonable request.

GDE preparation

The segregated GDLs were prepared by adding a MPL with high PTFE content onto a commercial carbon paper substrate (Fuel Cell Earth MGL190, 80190). A carbon and PTFE slurry was prepared by mixing 0.5 g of carbon black (Alfa Aesar, 39724), 5 g of 60 wt % PTFE dispersion (Sigma Aldrich, 665800), 5 drops of Triton X-100 (Sigma Aldrich, X100), 35 mL of isopropyl alcohol, and 5 g of deionized (DI) water. The carbon and PTFE slurry was blade-coated onto the MGL190 carbon paper with a blade height of 0.8 mm for 5 cm² experiments and 0.6 mm for 800 cm² experiments. The samples were left to dry at room temperature before the heat treatment in an oven. The oven was set to 180°C for 3 h to ensure that all the solvents had evaporated. The oven was then ramped to 280°C for 3 h to remove the surfactants. The oven was finally ramped to 340°C for 1 h to sinter the PTFE.

A Cu nanoparticle catalyst ink was prepared by mixing Cu nanoparticles (Sigma Aldrich, 774081) and Nafion D521 dispersion (Fuel Cell Store, 72500222) in methanol with a weight ratio of 2.6% and 4.7%, respectively. A carbon nanoparticle ink was prepared by mixing carbon black (Alfa Aesar, 39724) and Sustainion XA-9 ionomer (Dioxide Materials) in methanol with a weight ratio of 0.236% and 1.03%, respectively. The catalyst and carbon inks were sonicated for 1 h in an ultrasonic bath and deposited onto the GDL (using the same deposition for the commercial and the segregated GDLs, the commercial GDLs are listed in Table S1) with an airbrush until a loading of 1.5 and 0.1 mg/cm² were reached for the catalyst and carbon layers, respectively. The carbon nanoparticle layer was used to increase the stability of the Cu CL, similar to previous reports.[17,33,44]

MEA fabrication and electrochemical measurements

The CO₂RR electrochemical measurements were performed in a 5 cm² cell with a 316 stainless steel cathode and grade 2 titanium anode serpentine flow fields. The cell was assembled by sandwiching a 50 μm anion-exchange membrane (Sustainion X37–50 Grade RT, Dioxide Materials) between a cathode and an IrOx-coated titanium felt anode (Magneto Special Anodes). The cell was sealed with a 1/16″ o-ring placed into a machined groove in the anode flow field. The cell compression was achieved by tightening the cell with a torque screwdriver to 48 in oz.

Throughout all experiments, 40 sccm of humidified CO₂ (~100% relative humidity) at room temperature was fed to the cathode with a mass flow controller, and 10 mL/min of 0.1 M KHCO₃ was fed to the anode with a peristaltic pump. During all stability experiments, the cathode flow field was periodically rinsed with 5 mL of DI water for 1 min every 2 h using an automated peristaltic pump connected to the CO₂ inlet tube of the cell. The electrochemical measurements were performed with a potentiostat (Autolab PGSTAT204 with 10A booster) in galvanostatic mode. Each experiment was performed at room temperature without a break-in procedure, but the cell was left to stabilize for 1 h at each experimental condition before voltage

Joule
Article

measurements and gas samples were taken. The cell voltages were reported in all figures without iR correction.

The 800 and 8,000 cm^2 experiments were performed with 800 cm^2 titanium cells with parallel serpentine channel cathode and anode flow fields. A polyester support layer was added in between the IrOx and the anion-exchange membrane to minimize the chance of membrane punctures. The humidified CO_2 was sourced from amine-captured flue gas and was fed into the cell or cells with a thermal mass flow controller (Brooks Instruments SLA5861) at a rate of 0.7 and 3 kg/h in the 800 and 8,000 cm^2 experiments, respectively (photo of stack in Figure S21). The anolyte was fed at a rate of 1 L/min/cell, and it was cooled using a cooling loop to maintain the cell temperature at 40°C–45°C. An industrial power supply (FlexKraft) was used to maintain a constant current. The stack was operated in the monopolar configuration (each cell electrically in parallel) to ensure an equal distribution of voltage across all cells.

CO_2 reduction product analysis

The CO_2RR gas products were analyzed with a gas chromatograph (Clarus 590, Perkin Elmer) equipped with a thermal conductivity detector (TCD) and a flame ionization detector (FID). The gas chromatograph was equipped with a Molecular Sieve 5A capillary column and a packed Carboxen-1,000 column with argon as the carrier gas. The volumetric gas flow rates were measured with a bubble column.

The CO_2RR liquid products from the anode side of the cell were collected by taking a sample of the electrolyte after the operation and from the cathode side of the cell by condensing the vapors from the cathode gas stream with a cold trap. The electrolyte was replaced between each operating point in the experiment to determine the liquid product FE accurately. The liquid products were measured using proton nuclear magnetic resonance spectroscopy ($1H^+$ NMR) with an Agilent DD2 500 spectrometer in water suppression mode. The samples were diluted in D_2O, and dimethyl sulfoxide (DMSO) was used as the internal standard.

The FE of each gas product was calculated as follows: $FE_{gas} = x_i \cdot v \cdot \frac{z_i FP_0}{RT} \cdot \frac{1}{I_{total}} \cdot 100\%$

The FE of each liquid product was calculated as follows: $FE_{liquids} = n_i \cdot \frac{z_i F}{Q} \cdot 100\%$ where x_i represents the volume fraction of gas product i, v represents the gas flow rate at the outlet in sccm, z_i represents the number of electrons required to produce one molecule of product i, F represents the Faraday constant, P_0 is 101325 Pa, R represents the ideal gas constant, T represents the temperature, and I_{total} represents the total current; n_i represents the number of moles of product i, and Q represents the charge passed while the liquid products are being collected.

SEM analysis

All FIB and SEM work was conducted on a ZEISS Crossbeam 540 FIB/SEM. The sample preparation for the embedded cross-section mirrors the procedure published previously.[45–47] The sample preparation procedure for surface images, FIB sections, and FIB serial sections is explained in detail in a previous report.[48] A notable deviation is the use of a gold sputter coater (Cressington 108 manual) instead of a carbon coater.

MicroCT and segmentation

Data acquisition for the X-ray tomography was carried out by RJL Micro&Analytic using a Bruker SkyScan2211 device.

Joule
Article

The segmentation procedure builds on a previously published procedure.[28] The dataset was split into two parts to separate the part dominated by the MPL and CL from the part dominated by the fibers of the GDL. For each part, the segmentation was carried out by a UNET3D AI-segmentation.[49] For the MPL/CL part, the copper domains and the MPL were distinguished. For the fiber domain of the GDL, both fiber and binder were initially segmented as one domain versus pore space. The fibers and binder were then distinguished in a second step using Geodict's BinderFind AI algorithm. No attempts were made at distinguishing the domains of the MPL, as this was already accomplished by the array tomography.

Array tomography

Array tomography was employed to gain a 3D reconstruction of the MPL. A new approach to array tomography was developed, which is based on the physical sectioning of the sample, collection of the sequential sections on a substrate suitable for electron microscopy, and finally, imaging to generate a tomogram of the sample. A combination of SEM and EDX spectroscopy mapping was used for the imaging step. The processing steps for this procedure are described below.

Sample preparation

A thin layer (approximately 15 μm) of Nafion was deposited on the CL of the GDE to enhance the EDX contrast between carbon within the MPL and the epoxy resin used for embedding the sample. Then, the sample was embedded in Araldite 502 epoxy resin as preparation for ultramicrotomy. Sectioning was performed with an ATUMtome (RMC Boeckeler). The sample was cut using a Diatome histo diamond knife and collected on an aluminum-coated PET tape (Goodfellow ES301955) using the automated serial sectioning operation of the ATUMtome. Semi-thin sections were cut at a nominal thickness of 400 nm. A series of 410 sections (approx. 160 μm total cutting feed) was acquired.

Imaging of the sections

The tape with the collected sections was cut into strips and attached to aluminum tape holders (GP20334, Plano GmbH) using conductive carbon tape (G3939, Plano GmbH). We then coated the samples with a thin layer of carbon to ensure sufficient conductivity of the sample using a carbon coater (Balzers Union, MED 010).

We recorded the EDX maps using an XMAX-150 silicon drift detector (Oxford Instruments). The Aztec software of the same vendor was used in order to process the data. Additionally, we recorded images using the energy-selective backscatter detector (ESB) and the secondary electron detector (SE) of the microscope. The beam's acceleration voltage and current were 5 kV and 2 nA, respectively. The acquisition resolution was 1,024 × 768 pixels, and the pixel dwell time was 200 μs. These values represent a compromise between acquisition time and resolution. The field of view for imaging was adjusted to have the bottom of each section level with the imaging plane.

Reconstruction

The 3D reconstruction of the original sample volume followed a multi-step process. First, a segmentation based on the Otsu method was performed for the EDX-intensity mappings of the fluorine signal. The resulting image stack was scaled to 0.25 times the original size in X and Y directions to accelerate the following intensity-based image registration. Image registration was performed to compensate for offsets in the fields of view between the single sections of the image stack. Rigid image registration was performed in MATLAB, which restricted the alignment to translation

and rotation of subsequent images, and it was performed relative to the previous image sequentially throughout the whole image stack. The resulting correction was then applied to original-sized image stacks of EDX mappings as well as of SE- and energy selective backscatter (ESB)-images.

Next, section compression and anisotropic voxel sizes were corrected. The surface area of the sections was compared with the surface area of the block face of the remaining sample after serial sectioning. The difference between them was used to compensate for section compression, which was identified as 0.75 of the block face length. EDX mappings had an original pixel size of 300 nm; SE and ESB images of 150 nm. The tomograms were interpolated to a final, isotropic voxel size of 400 nm to match the lower z-resolution that was defined by the section thickness.

The final segmentation of the fluorine-EDX-tomogram was performed using ImageJ. An Otsu-based threshold segmentation of the EDX mappings of the fluorine signal was performed after image processing (contrast enhancement by multiplication of raw data with data after application of a Gaussian blur filter (size 2) and 3D median filtering to minimize noise).

FIB/SEM tomography

Microscope and sample preparation for FIB/SEM serial section are as described above for the SEM work. The data acquisition was carried out using the ATLAS software and scan generator. An accelerating voltage of 3 kV and a probe current of 2 nA were used. A pixel size of 4 nm was selected along with a targeted slice thickness of 12 nm. The actual average slice thickness was found to be 12.41 nm. Slice alignment was carried out in MATLAB using a previously published procedure.[48,50] However, the shifting was performed using by taking into account the observed slicing distance as opposed to the average.

Segmentation and reconstruction

The segmentation of the FIB/SEM data was carried out as an iterative, multistage process in GeoDict. Initial identification of the principal regions (Pt protective layer, CL, porous carbon domain, and PTFE domain) was carried out using the UNET3D AI-based algorithm. The subsequent segmentation of the porous structures was carried out using an optical flow-based algorithm[50] in the same manner as previously described.[48] The resulting structures were resampled to have cubic voxels of 8 nm edge length.

Analysis of the tomographic data

The dimensions and resolutions of the three reconstructions and all the relevant sub-volumes are indicated in Table S5 in the supplemental information. Pore-size and grain-size distributions were calculated as granulometries using GeoDict's PoroDict and MatDict packages and are stated in terms of pore/grain diameters.

The transport simulations were performed using DiffuDict, ConductoDict, and FlowDict packages of GeoDict. Continuum transport simulations were carried out using the LIR PDE solvers for Fick's first law, the Stokes equation, and Ohm's law, respectively. Knudsen diffusion was calculated by Monte Carlo methods. A more detailed discussion of the equations and the boundary conditions can be found in our previous publication.[28] A brief summary of the equations involved can be found in the supplemental information in Table S6. Table S6 also features a definition of the relative diffusivities and conductivities with respect to the effective parameters. The data for the porous carbon were calculated from 3 volumes (Figure S14). The

Joule
Article

CellPress
OPEN ACCESS

transport data for the MPL are averaged from 4 volumes (Figure S8). The analysis of the copper CL posed a challenge, as the analysis algorithms require box-shaped volumes. 10 box-shaped volumes were extracted from the CL for analysis. These sub-volumes are shown in Figure S6. The given transport parameters are calculated as a volume-weighted average. Laplace, Knudsen, and Bosanquet effective diffusion coefficients for CO_2 were calculated using a mean thermal velocity of 375 m/s.[51] The errors are estimated as (weighted) standard deviations from the mean.

SUPPLEMENTAL INFORMATION

Supplemental information can be found online at https://doi.org/10.1016/j.joule. 2024.07.004.

AUTHOR CONTRIBUTIONS

C.P.O. designed and carried out all experiments, as well as prepared the manuscript. D.M. performed tomographic analysis and prepared the manuscript. T.B. assisted with data analysis and manuscript preparation. All authors discussed the results and assisted during the manuscript preparation. D.S. and S.T. supervised the project.

DECLARATION OF INTERESTS

The authors declare the following competing financial interest(s): there is a patent application pending on the GDE structure described here, filed by the authors of this paper and their institutions. C.P.O., C.M.G., J.P.E., D.Y., and D.S. are employees and/or shareholders of CERT Systems Inc, a company commercializing CO_2 electrolysis technology.

REFERENCES

1. Bushuyev, O.S., De Luna, P., Dinh, C.T., Tao, L., Saur, G., van de Lagemaat, J., Kelley, S.O., and Sargent, E.H. (2018). What Should We Make with CO2 and How Can We Make It? Joule 2, 825–832. https://doi.org/10.1016/j.joule.2017.09.003.

2. Jouny, M., Luc, W., and Jiao, F. (2018). General Techno-Economic Analysis of CO2 Electrolysis Systems. Ind. Eng. Chem. Res. 57, 2165–2177. https://doi.org/10.1021/acs.iecr.7b03514.

3. Shin, H., Hansen, K.U., and Jiao, F. (2021). Techno-economic assessment of low-temperature carbon dioxide electrolysis. Nat. Sustain. 4, 911–919. https://doi.org/10.1038/s41893-021-00739-x.

4. Verma, S., Kim, B., Jhong, H.R.M., Ma, S., and Kenis, P.J.A. (2016). A gross-margin model for defining technoeconomic benchmarks in the electroreduction of CO2. ChemSusChem 9, 1972–1979. https://doi.org/10.1002/cssc.201600394.

5. Rabiee, H., Ge, L., Zhang, X., Hu, S., Li, M., and Yuan, Z. (2021). Gas diffusion electrodes (GDEs) for electrochemical reduction of carbon dioxide, carbon monoxide, and dinitrogen to value-added products: A review. Energy Environ. Sci. 14, 1959–2008. https://doi.org/10.1039/d0ee03756g.

6. Martín, A.J., Larrazábal, G.O., and Pérez-Ramírez, J. (2015). Towards sustainable fuels and chemicals through the electrochemical reduction of CO 2: lessons from water electrolysis. Green Chem. 17, 5114–5130. https://doi.org/10.1039/c5gc01893e.

7. Kutz, R.B., Chen, Q., Yang, H., Sajjad, S.D., Liu, Z., and Masel, I.R. (2017). Sustainion Imidazolium-Functionalized Polymers for Carbon Dioxide Electrolysis. Energy Tech. 5, 929–936. https://doi.org/10.1002/ente.201600636.

8. Liu, Z., Yang, H., Kutz, R., and Masel, R.I. (2018). CO2 electrolysis to CO and O2 at high selectivity, stability and efficiency using sustainion membranes. J. Electrochem. Soc. 165, J3371–J3377. https://doi.org/10.1149/2.0501815jes.

9. Haas, T., Krause, R., Weber, R., Demler, M., and Schmid, G. (2018). Technical photosynthesis involving CO2 electrolysis and fermentation. Nat. Catal. *1*, 32–39. https://doi.org/10.1038/s41929-017-0005-1.

10. Krause, R., Reinisch, D., Reller, C., Eckert, H., Hartmann, D., Taroata, D., Wiesner-Fleischer, K., Bulan, A., Lueken, A., and Schmid, G. (2020). Industrial Application Aspects of the Electrochemical Reduction of CO2 to CO in Aqueous Electrolyte. Chem. Ing. Tech. *92*, 53–61. https://doi.org/10.1002/cite.201900092.

11. Jeanty, P., Scherer, C., Magori, E., Wiesner-Fleischer, K., Hinrichsen, O., and Fleischer, M. (2018). Upscaling and continuous operation of electrochemical CO2 to CO conversion in aqueous solutions on silver gas diffusion electrodes. J. CO2 Util. *24*, 454–462. https://doi.org/10.1016/j.jcou.2018.01.011.

12. Nwabara, U.O., Cofell, E.R., Verma, S., Negro, E., and Kenis, P.J.A.A. (2020). Durable Cathodes and Electrolyzers for the Efficient Aqueous Electrochemical Reduction of CO2. ChemSusChem *13*, 855–875. https://doi.org/10.1002/cssc.201902933.

13. Xu, Y., Miao, R.K., Edwards, J.P., Liu, S., O'Brien, C.P., Gabardo, C.M., Fan, M., Huang, J.E., Robb, A., Sargent, E.H., and Sinton, D. (2022). A microchanneled solid electrolyte for carbon-efficient CO2 electrolysis. Joule *6*, 1333–1343. https://doi.org/10.1016/j.joule.2022.04.023.

14. Li, F., Thevenon, A., Rosas-Hernández, A., Wang, Z., Li, Y., Gabardo, C.M., Ozden, A., Dinh, C.T., Li, J., Wang, Y., et al. (2020). Molecular tuning of CO2-to-ethylene conversion. Nature *577*, 509–513. https://doi.org/10.1038/s41586-019-1782-2.

15. Masel, R.I., Liu, Z., Yang, H., Kaczur, J.J., Carrillo, D., Ren, S., Salvatore, D., and Berlinguette, C.P. (2021). An industrial perspective on catalysts for low-temperature CO2 electrolysis. Nat. Nanotechnol. *16*, 118–128. https://doi.org/10.1038/s41565-020-00823-x.

16. Kovalev, M.K., Ren, H., Zakir Muhamad, M., Ager, J.W., and Lapkin, A.A. (2022). Minor Product Polymerization Causes Failure of High-Current CO 2-to-Ethylene Electrolyzers. ACS Energy Lett. *7*, 599–601. https://doi.org/10.1021/acsenergylett.1c02450.

17. Dinh, C.-T.T., Burdyny, T., Kibria, M.G., Seifitokaldani, A., Gabardo, C.M., García de Arquer, F.P., Kiani, A., Edwards, J.P., De Luna, P., Bushuyev, O.S., et al. (2018). CO2 electroreduction to ethylene via hydroxide-mediated copper catalysis at an abrupt interface. Science *360*, 783–787. https://doi.org/10.1126/science.aas9100.

18. Xu, Y., Edwards, J.P., Liu, S., Miao, R.K., Huang, J.E., Gabardo, C.M., O'Brien, C.P., Li, J., Sargent, E.H., and Sinton, D. (2021). Self-Cleaning CO2 Reduction Systems: Unsteady Electrochemical Forcing Enables Stability. ACS Energy Lett. *6*, 809–815. https://doi.org/10.1021/acsenergylett.0c02401.

19. Nwabara, U.O., Hernandez, A.D., Henckel, D.A., Chen, X., Cofell, E.R., De-Heer, M.P., Verma, S., Gewirth, A.A., and Kenis, P.J.A. (2021). Binder-Focused Approaches to Improve the Stability of Cathodes for CO2 Electroreduction. ACS Appl. Energy Mater. *4*, 5175–5186. https://doi.org/10.1021/acsaem.1c00715.

20. Cofell, E.R., Nwabara, U.O., Bhargava, S.S., Henckel, D.E., and Kenis, P.J.A.A. (2021). Investigation of electrolyte-dependent carbonate formation on gas diffusion electrodes for CO2 electrolysis. ACS Appl. Mater. Interfaces *13*, 15132–15142. https://doi.org/10.1021/acsami.0c21997.

21. Endrődi, B., Samu, A., Kecsenovity, E., Halmágyi, T., Sebők, D., and Janáky, C. (2021). Operando cathode activation with alkali metal cations for high current density operation of water-fed zero-gap carbon dioxide electrolysers. Nat. Energy *6*, 439–448. https://doi.org/10.1038/s41560-021-00813-w.

22. Leonard, M.E., Orella, M.J., Aiello, N., Román-Leshkov, Y., Forner-Cuenca, A., and Brushett, F.R. (2020). Editors' Choice—Flooded by Success: On the Role of Electrode Wettability in CO 2 Electrolyzers that Generate Liquid Products. J. Electrochem. Soc. *167*, 124521. https://doi.org/10.1149/1945-7111/abaa1a.

23. Yang, K., Kas, R., Smith, W.A., and Burdyny, T. (2021). Role of the carbon-based gas diffusion layer on flooding in a gas diffusion electrode cell for electrochemical CO2 reduction. ACS Energy Lett. *6*, 33–40. https://doi.org/10.1021/acsenergylett.0c02184.

24. Thiele, S., Zengerle, R., and Ziegler, C. (2011). Nano-morphology of a polymer electrolyte fuel cell catalyst layer-imaging, reconstruction and analysis. Nano Res. *4*, 849–860. https://doi.org/10.1007/s12274-011-0141-x.

25. Vierrath, S., Güder, F., Menzel, A., Hagner, M., Zengerle, R., Zacharias, M., and Thiele, S. (2015). Enhancing the quality of the tomography of nanoporous materials for better understanding of polymer electrolyte fuel cell materials. J. Power Sources *285*, 413–417. https://doi.org/10.1016/j.jpowsour.2015.03.110.

26. Hegge, F., Moroni, R., Trinke, P., Bensmann, B., Hanke-Rauschenbach, R., Thiele, S., and Vierrath, S. (2018). Three-dimensional microstructure analysis of a polymer electrolyte membrane water electrolyzer anode. J. Power Sources *393*, 62–66. https://doi.org/10.1016/j.jpowsour.2018.04.089.

27. Jhong, H.R., Brushett, F.R., and Kenis, P.J.A. (2013). The effects of catalyst layer deposition methodology on electrode performance. Adv. Energy Mater. *3*, 589–599. https://doi.org/10.1002/aenm.201200759.

28. McLaughlin, D., Bierling, M., Mayerhöfer, B., Schmid, G., and Thiele, S. (2023). Digital Twin of a Hierarchical CO2 Electrolyzer Gas Diffusion Electrode. Adv. Funct. Mater. *33*, 2212462. https://doi.org/10.1002/adfm.202212462.

29. Klingele, M., Moroni, R., Vierrath, S., and Thiele, S. (2018). Multiscale Tomography-Based Analysis of Polymer Electrolyte Fuel Cells: Towards a Fully Resolved Gas Diffusion Electrode Reconstruction. J. Electrochem. Energy Convers. Storage *15*, 1–7. https://doi.org/10.1115/1.4037244.

30. Zielke, L., Hutzenlaub, T., Wheeler, D.R., Chao, C.W., Manke, I., Hilger, A., Paust, N., Zengerle, R., and Thiele, S. (2015). Three-phase multiscale modeling of a LiCoO2 cathode: Combining the advantages of FIB-SEM imaging and X-ray tomography. Adv. Energy Mater. *5*, 1401612. https://doi.org/10.1002/aenm.201401612.

31. Zielke, L., Hutzenlaub, T., Wheeler, D.R., Manke, I., Arlt, T., Paust, N., Zengerle, R., and Thiele, S. (2014). A combination of X-ray tomography and carbon binder modeling: Reconstructing the three phases of LiCoO2 Li-ion battery cathodes. Adv. Energy Mater. *4*, 2–7. https://doi.org/10.1002/aenm.201301617.

32. García de Arquer, F.P., Dinh, C.-T.T., Ozden, A., Wicks, J., McCallum, C., Kirmani, A.R., Nam, D.-H.H., Gabardo, C., Seifitokaldani, A., Wang, X., et al. (2020). CO2 electrolysis to multicarbon products at activities greater than 1 A cm− 2. Science *367*, 661–666. https://doi.org/10.1126/science.aay4217.

33. Gabardo, C.M., O'Brien, C.P., Edwards, J.P., McCallum, C., Xu, Y., Dinh, C.-T.T., Li, J., Sargent, E.H., Sinton, D., and O'Brien, C.P. (2019). Continuous Carbon Dioxide Electroreduction to Concentrated Multi-carbon Products Using a Membrane Electrode Assembly. Joule *3*, 2777–2791. https://doi.org/10.1016/j.joule.2019.07.021.

34. Wicks, J., Jue, M.L., Beck, V.A., Oakdale, J.S., Dudukovic, N.A., Clemens, A.L., Liang, S., Ellis, M.E., Lee, G., Baker, S.E., et al. (2021). 3D-Printable Fluoropolymer Gas Diffusion Layers for CO2 Electroreduction. Adv. Mater. *33*, e2003855. https://doi.org/10.1002/adma.202003855.

35. Moradzaman, M., Martínez, C.S., and Mul, G. (2020). Effect of partial pressure on product selectivity in Cu-catalyzed electrochemical reduction of CO2. Sustain. Energ. Fuels *4*, 5195–5202. https://doi.org/10.1039/D0SE00865F.

36. McCallum, C., Gabardo, C.M., O'Brien, C.P., Edwards, J.P., Wicks, J., Xu, Y., Sargent, E.H., Sinton, D., O'Brien, C.P., Edwards, J.P., et al. (2021). Reducing the crossover of carbonate and liquid products during carbon dioxide electroreduction. Cell Rep. Phys. Sci. *2*, 100522. https://doi.org/10.1016/j.xcrp.2021.100522.

37. Garg, S., Giron Rodriguez, C.A.G., Rufford, T.E., Varcoe, J.R., and Seger, B. (2022). How membrane characteristics influence the performance of CO2 and CO electrolysis. Energy Environ. Sci. *15*, 4440–4469. https://doi.org/10.1039/d2ee01818g.

38. Salvatore, D.A., Gabardo, C.M., Reyes, A., O'Brien, C.P., Holdcroft, S., Pintauro, P., Bahar, B., Hickner, M., Bae, C., Sinton, D., et al. (2021). Designing anion exchange membranes for CO 2 electrolysers. Nat. Energy *6*, 339–348. https://doi.org/10.1038/s41560-020-00761-x.

39. Reyes, A., Jansonius, R.P., Mowbray, B.A.W., Cao, Y., Wheeler, D.G., Chau, J., Dvorak, D.J., and Berlinguette, C.P. (2020). Managing Hydration at the Cathode Enables Efficient CO2 Electrolysis at Commercially Relevant Current Densities. ACS Energy Lett. *5*, 1612–1618. https://doi.org/10.1021/acsenergylett.0c00637.

40. Leonard, M.E., Clarke, L.E., Forner-Cuenca, A., Brown, S.M., and Brushett, F.R. (2020). Investigating Electrode Flooding in a Flowing

Electrolyte, Gas-Fed Carbon Dioxide Electrolyzer. ChemSusChem *13*, 400–411. https://doi.org/10.1002/cssc.201902547.

41. Weng, L.-C.C., Bell, A.T., and Weber, A.Z. (2019). Towards membrane-electrode assembly systems for CO2 reduction: A modeling study. Energy Environ. Sci. *12*, 1950–1968. https://doi.org/10.1039/c9ee00909d.

42. Weng, L.C., Bell, A.T., and Weber, A.Z. (2018). Modeling gas-diffusion electrodes for CO2 reduction. Phys. Chem. Chem. Phys. *20*, 16973–16984. https://doi.org/10.1039/c8cp01319e.

43. Bui, J.C., Lees, E.W., Pant, L.M., Zenyuk, I.V., Bell, A.T., and Weber, A.Z. (2022). Continuum Modeling of Porous Electrodes for Electrochemical Synthesis. Chem. Rev. *122*, 11022–11084. https://doi.org/10.1021/acs.chemrev.1c00901.

44. Ozden, A., Li, F., García de Arquer, F.P., Rosas-Hernández, A., Thevenon, A., Wang, Y., Hung, S.-F.F., Wang, X., Chen, B., Li, J., et al. (2020). High rate and efficient ethylene electrosynthesis using a catalyst/promoter/transport layer. ACS Energy Lett. *5*, 2811–2818.

https://doi.org/10.1021/acsenergylett.0c01266.

45. Seeberger, D., McLaughlin, D., Hauenstein, P., and Thiele, S. (2020). Bipolar-interface fuel cells - an underestimated membrane electrode assembly concept for PGM-free ORR catalysts. Sustain. Energ. Fuels *4*, 2508–2518. https://doi.org/10.1039/d0se00288g.

46. Mayerhöfer, B., McLaughlin, D., Böhm, T., Hegelheimer, M., Seeberger, D., Thiele, S., Mayerhöfer, B., McLaughlin, D., Böhm, T., and Hegelheimer, M. (2020). Bipolar membrane electrode assemblies for water electrolysis. ACS Appl. Energy Mater. *3*, 9635–9644. https://doi.org/10.1021/acsaem.0c01127.

47. Bühler, M., Holzapfel, P., McLaughlin, D., and Thiele, S. (2019). From Catalyst Coated Membranes to Porous Transport Electrode Based Configurations in PEM Water Electrolyzers. J. Electrochem. Soc. *166*, F1070–F1078. https://doi.org/10.1149/2.0581914jes.

48. McLaughlin, D., Bierling, M., Moroni, R., Vogl, C., Schmid, G., and Thiele, S. (2020).

Tomographic Reconstruction and Analysis of a Silver CO2 Reduction Cathode. Adv. Energy Mater. *10*, 1–7. https://doi.org/10.1002/aenm.202000488.

49. Ronneberger, O., Fischer, P., and Brox, T. (2015). Medical Image Computing and Computer-Assisted Intervention - MICCAI 2015. In 18th International Conference Munich, Germany, October 5-9, 2015 proceedings, part III. In Lecture Notes in Computer Science (including subseries Lecture Notes in Artificial Intelligence and Lecture Notes in Bioinformatics), N. Navab, J. Hornegger, W.M. Wells, and A.F. Frangi, eds. (Springer), p. 234. https://doi.org/10.1007/978-3-319-24574-4.

50. Moroni, R., and Thiele, S. (2020). FIB/SEM tomography segmentation by optical flow estimation. Ultramicroscopy *219*, 113090. https://doi.org/10.1016/j.ultramic.2020.113090.

51. Wutz, M., Adam, H., Walcher, W., and Jouston, K. (2000). Handbuch Vakuumtechnik – Theorie und Praxis, Seventh Edition (Vieweg).